Program Digest, 2019 IEEE International Ultrasonics Symposium (IUS)
Glasgow, Scotland, October 6-9, 2019

5 GHz Acoustic Delay Lines using Antisymmetric Mode in Lithium Niobate Thin Film

Ruochen Lu, Yansong Yang, Michael Breen, Ming-Huang Li, and Songbin Gong
Department of Electrical and Computer Engineering
University of Illinois at Urbana-Champaign, Urbana, IL
rlu10, yyang165, mgbreen2, mhli, songbin@illinois.edu

***Abstract*—This paper demonstrates the first group of acoustic delay lines (ADLs) at 5 GHz, using the first-order antisymmetric (A1) mode in Z-cut lithium niobate thin films. Thanks to the fast phase velocity, large coupling coefficient, and low-loss of A1 waves, the implemented ADLs significantly surpass the operation frequency of precious works with similar feature sizes. The impact of the key design parameters on the device performance is first discussed. The implemented ADLs at 5 GHz show a minimum insertion loss of 7.9 dB, and delays ranging between 15 ns and 109 ns over a fractional bandwidth around 4%. The propagation characteristics of A1 mode acoustic waves have also been extracted for the first time. The A1 ADLs can potentially enable wideband high-frequency passive signal processing functions for future 5G applications in the sub-6 GHz spectrum bands.**

Keywords*—*Acoustic delay line, lithium niobate, microelectromechanical systems, A1 mode, piezoelectricity

I. Introduction

The fifth-generation (5G) New Radio (NR) is calling for microsystems that can either provide conventional signal processing functions with better performance or accomplish new tasks for emerging applications [1]. The enhanced mobile broadband (eMBB), as one crucial 5G NR application scenario targeting at a thousand-fold increase in the mobile data volume per unit [2], requires wideband, efficient, and compact signal processing elements at radio frequency (RF). Acoustic signal processing, where the electromagnetic (EM) signals are transduced and processed in the acoustic domain, is a promising candidate for miniature, low-loss, wideband signal processing functions. First, the acoustic devices are desirable for handheld applications requiring compact footprints because the acoustic wavelengths are five orders of magnitude smaller than the EM counterparts at the same frequency [3]. Second, diverse analog processing functions can be passively implemented in the acoustic domain [4]–[8], which does not compete against the analog-to-digital converters (ADC) and the following digital processors for the stringent power budget in the RF front-ends. Third, the recent demonstrations of low-loss and high electromechanical coupling (k^2) acoustic platforms enable devices with lower insertion loss (IL) and larger fractional bandwidth (FBW) [9]–[13], which can potentially overcome the current performance bottlenecks hindering acoustic signal processing from eMBB applications.

Among different acoustic devices, acoustic delay lines (ADLs) have been demonstrated with various applications, ranging from transversal filters [14], [15], correlators [16], to the emerging prototypes of amplifiers [17], [18] and time-varying non-reciprocal systems [19]. The conventional ADLs are built upon surface acoustic wave (SAW) platforms [14]. Despite the successful demonstrations at lower frequencies, scaling the operation frequencies above 3 GHz is challenging for two reasons. First, the slow phase velocity (v_p) limits the maximum operating frequencies, unless narrow electrodes (<300 nm), intrinsically lossy modes, or thin films on costly substrates are used [9]. Second, moderate k^2 fundamentally limits the design trades in IL versus FBW [14], [20]. In other words, wide FBW is only achievable at the cost of significant IL.

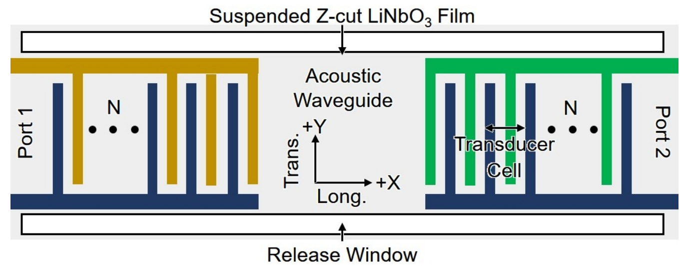

Fig. 1. Mockup of an A1 ADL on a suspended Z-cut LiNbO3 thin film.

Recently, ADLs have been demonstrated with low-loss and wideband performance using the fundamental shear horizontal (SH0) mode [21] and fundamental symmetrical (S0) mode [22] in single-crystal lithium niobate ($LiNbO_3$) thin films. The enhanced performance is enabled by the large k^2 and low-loss of SH0 and S0 in $LiNbO_3$ [11], [23], [24]. Nevertheless, v_p of these modes are still inadequate for enabling acoustic signal processing at the planned eMBB bands near 5 GHz [2]. To this end, the first-order antisymmetric (A1) mode in Z-cut $LiNbO_3$ is a promising candidate for eMBB applications, because of its demonstrated simultaneously fast v_p, high k^2, and low loss [25]–[29]. However, the highly dispersive nature of A1 presents new challenges in designing ADLs, namely the notable cut-off phenomenon. Because A1 is higher-order in the thickness direction, acoustic waves below the cut-off frequency are confined within the input transducers. Therefore, the successful implementation of A1 ADLs relies on both systematic analysis of the A1 dispersion, and understanding of the effects of key ADL parameters. In this work, we aim to demonstrate the first group of A1 ADLs in Z-cut $LiNbO_3$. Based on the analysis of A1 in $LiNbO_3$ and the key design parameters, A1 ADLs are in-house fabricated. The implemented ADLs at 5 GHz show a minimum insertion loss of 7.9 dB, and a fractional bandwidth around 4%, with delays ranging between 15 ns and 109 ns. The demonstrated devices can unlock new possibilities for acoustic signal processing for 5G eMBB applications.

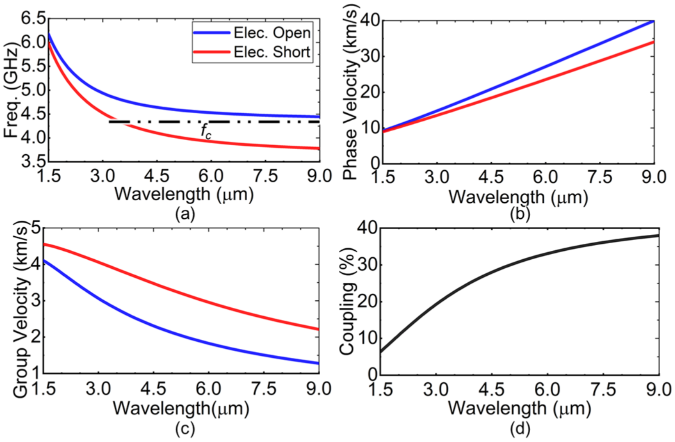

Fig. 2. Simulated dispersion characteristics of A1 with different wavelengths in a 0.49 μm thick Z-cut LiNbO3 thin film. (a) Frequency, (b) v_p, and (c) v_g with electrically open and short boundary conditions. (d) k^2 at different wavelength.

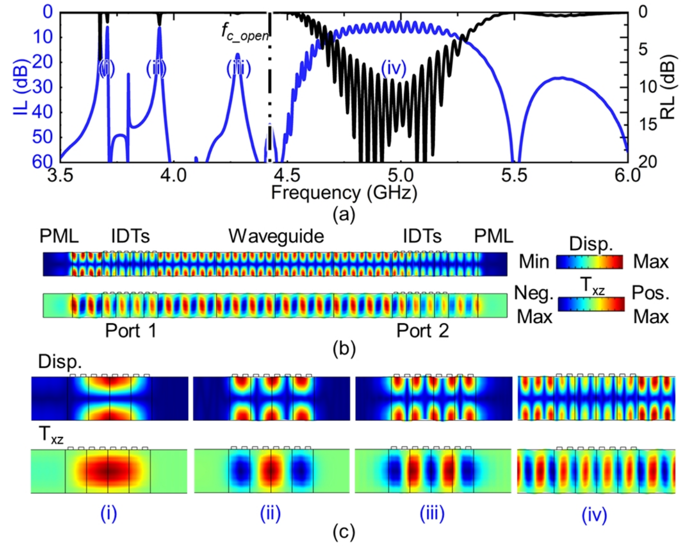

Fig. 3. (a) Simulated IL and RL with both ports conjugately matched. The evanescent modes in the input transducers are labeled. (b) Displacement and T_{xz} stress distribution at the center frequency. (c) Displacement mode shapes and stress distributions in the input transducers at the marked frequencies.

II. Design and Simulation

The schematic of a typical A1 ADL is presented in Fig. 1. The ADL is composed of 30 nm aluminum interdigitated transducers (IDTs) on a suspended 490 nm Z-cut $LiNbO_3$ thin film. The thickness of the thin film is chosen for enabling wideband response at 5 GHz. A pair of bi-directional transducers are placed on the opposite ends of the ADL. The transducers are composed of N pairs of cascaded transducer unit cells. Each cell has a length of Λ, over which is situated a pair of transduction electrodes (each $\Lambda/4$ wide) with separations of $\Lambda/4$ in between. The electrodes are alternatingly connected to signal (orange IDTs for Port 1, green IDTs for Port 2) and ground (blue IDTs). The wave propagation direction is orientated along the material's X-axis to minimize the power flow angle (PFA) for reducing energy dissipation [22]. Free boundaries (i.e., etch windows) are defined in the transverse direction of the acoustic waveguide. In operation, the EM signals are sent to the piezoelectric transducers at Port 1 and converted into acoustic waves. The launched acoustic waves propagate toward both ends, therefore sending half of the power toward Port 2. Similarly, after traversing through the waveguide with a gap length of L_g, only half of the power launched toward Port 2 is collected, causing a minimum IL of 6 dB. Various acoustic signal processing functions can be passively implemented through designing the transducers [16] and the waveguide [6].

To circumvent the cut-off issue, the dispersion relations of A1 waves in a Z-cut $LiNbO_3$ thin film is analyzed using COMSOL finite element analysis (FEA). Eigenmode simulation is set up for a 490 nm Z-cut $LiNbO_3$ thin film section with different width (wavelength, λ) between 1.5 μm and 9.0 μm. Periodic boundary conditions (in both the electrical and mechanical domains) are applied to the XZ and YZ planes. The XY planes are set as mechanically free. The electrical boundary conditions of the XY planes are set to be electrically open and short, respectively [22]. The simulated A1 dispersion curves are presented in Fig. 2 (a). The frequency of the electrically short case is lower than that of the electrically open case for the same λ due to the piezoelectric softening effect. The frequency decreases with a longer λ. However, different from the SH0 [21] and S0 [22] cases, the frequency of A1 is always higher than a certain frequency, namely the cut-off frequency [25]. More specifically, a cut-off frequency for the electrically short case (f_{c_short}) of 3.66 GHz and a cut-off frequency for the electrically open case (f_{c_open}) of 4.37 GHz are observed. To enable the traveling A1 waves, the devices have to operate beyond f_{c_open}. Otherwise, A1 waves cannot propagate without significant attenuation. From the dispersion curves, three key parameters, namely the phase velocity v_p, the group velocity v_g, and the electromechanical coupling coefficient k^2 are calculated as [30]:

$$v_p = f\lambda \tag{1}$$

$$v_g = v_p - \lambda \cdot dv_p/d\lambda \tag{2}$$

$$k^2 = (v_f^2 - v_m^2)/v_m^2 \tag{3}$$

where f is the center frequency. v_f and v_m are the phase velocities with electrically free and open boundary conditions, respectively. A remarkably high v_p over 9000 m/s is obtained for A1 below 6.5 GHz [Fig. 2 (b)], indicating that 5 GHz devices can be achieved with λ around 2.4 μm (i.e., a feature size of 600 nm). A low v_g below 4500 m/s is also observed [Fig. 2 (c)], showing that a significant delay can be obtained within a compact structure. High k^2 over 40% can be observed for A1 waves with a long λ [Fig. 2 (d)]. k^2 declines for A1 waves at a higher frequency. Nevertheless, k^2 around 15% can be obtained for 5 GHz devices (λ of 2.4 μm), showing the potential of constructing low IL, large FBW ADLs for eMBB applications.

The typical response of an A1 ADL is then studied using 2D FEA [22]. The 2D FEA assumes that the acoustic waves are plane waves propagating along the X-axis shown in Fig. 1, neglecting the fridge effects near the release windows. Three key dimensions determine the ADL specifications. First, the gap length L_g determines the obtained group delay δ. Second, the cell length Λ determines the center frequency f_{center} of the passband. Third, the cell number N affects the FBW of the passband. Without loss of generality, an A1 ADL prototype (cell length Λ = 2.4 μm, gap length L_g = 40 μm, cell number

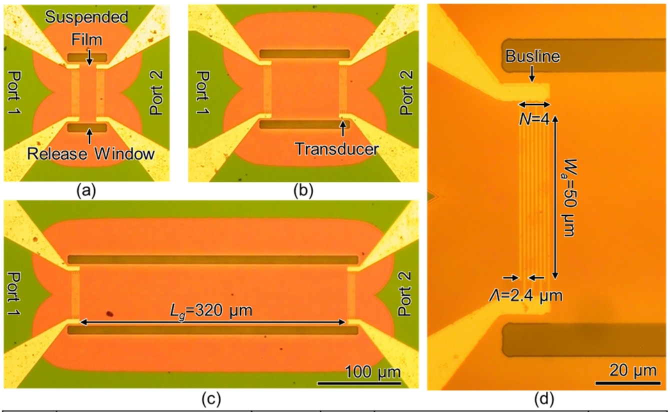

Sym.	Parameter	Value	Sym.	Parameter	Value
Λ	Cell length (μm)	2.4	W_a	Aperture width (μm)	50
N	Number of cells	4	W_d	Device width (μm)	74
L_g	Gap length (μm)	20-320	L_T	Transducer length (μm)	9.6
T_{LN}	LiNbO3 thickness (nm)	490	T_{Al}	Aluminum thickness (nm)	30

Fig. 4. Optical microscope images of the fabricated ADLs. Zoomed-out images of A1 ADLs with L_g of (a) 20, (b) 80, and (c) 320 μm. (d) Zoomed-in image of a transducer with 4 cells.

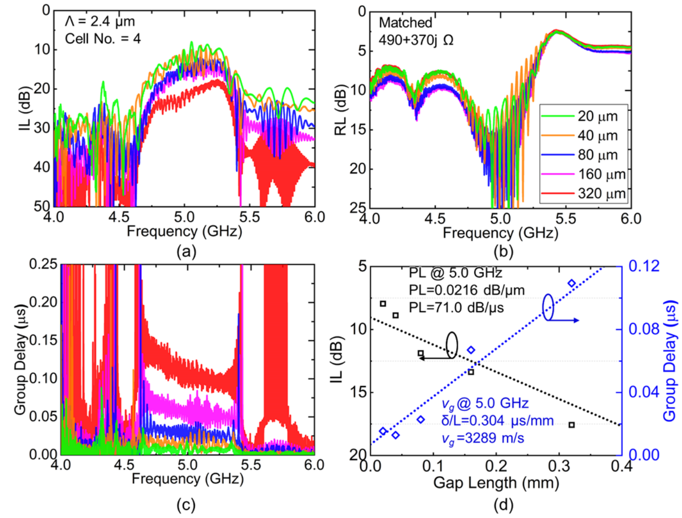

Fig. 5. Measured S-parameters of the A1 ADLs with identical transducers (N=4, Λ=2.4 μm) but different L_g (20 – 320 μm). (a) IL, (b) RL, and (c) group delay responses. (d) Extracted propagation loss (71 dB/μs), and group velocity (3289 m/s) of A1 at 5.0 GHz.

N = 4, and aperture width 50 μm) is simulated to showcase the operating principles of A1 ADLs (Fig. 3). The S-parameters are obtained from the frequency domain FEA and then conjugately matched with 360 + j30 Ω for both the input and output ports [Fig. 3 (a)], showing a well-defined passband centered around 5 GHz. The displacement mode shape and the stress distribution (T_{xz}) at the center frequency are plotted in Fig. 3 (b). The minimum in-band IL is 3.7 dB, among which 6-dB IL is caused by the bi-directional loss. The slight ripples in RL and IL are caused by triple transit signals (TTS) between the input and output transducers. Different from S0 and SH0 ADLs, the A1 ADL features a non-symmetric passband, caused by the cut-off of A1 mode (f_{c_open} labeled in the figure). Below f_{c_open}, A1 waves are evanescent in $LiNbO_3$. Thus the amplitude decays during the propagation toward the output transducers. The resonant modes below f_{c_open} are marked with (i)-(iii) in the frequency response [Fig. 3 (a)]. Their displacement and stress mode shapes are shown in Fig. 3 (c). The acoustic vibrations are mostly confined between the input transducers, thus validating the cut-off theory.

III. Fabrication and Measurement

The devices were fabricated in-house with the process presented in [22]. A 490 nm Z-cut $LiNbO_3$ thin film on a 4-inch Si wafer is provided by NGK Insulators, Ltd., for the fabrication. The optical images of the fabricated ADLs are shown in Fig. 4. The key design parameters, namely Λ, L_g, and N are labeled, and their typical values are presented in the inset table. Five ADLs with the same transducer design (Λ of 2.4 μm and N of 4) but different L_g between 20 μm and 320 μm are fabricated, to showcase the operation principles of A1 ADLs and to identify the key propagation parameters.

The fabricated ADLs were first measured with a vector network analyzer (VNA) at the −10 dBm power level in air, and then conjugately matched. The measured IL and RL are shown in Fig. 5 (a)-(b) with the ports conjugately matched. The ADLs show a passband centered at 5.0 GHz. A minimum IL of 7.9 dB and an FBW around 4% have been achieved for the ADL with a 20 μm gap length. Delays between 15 ns and 109 ns are measured. An increase in IL is observed for longer ADLs, caused by the propagation loss (PL) of A1 in the $LiNbO_3$ waveguide. Larger transmission can be observed out of the passband for shorter devices, which is caused by the capacitive feedthrough between the ports. Ripples caused by the multi-reflection between ports and the internal reflections in the transducers are seen in the passband. The larger RL out of the passband is due to the series resistance in the electrodes. The non-propagating modes can be observed below the cut-off frequency in Fig. 5 (a), but they are significantly damped by PL. Dispersive group delays are observed for different devices, showing longer delays near the cut-off frequency as simulated in Fig. 2 (c). A1 propagation characteristics are extracted from the dataset, showing a PL of 71 dB/μs (or 0.0216 dB/μm), and v_g of 3289 m/s 5.0 GHz.

The wideband performance of A1 ADLs is presented in Fig. 6. The cut-off can be clearly identified below the f_{c_open} around 4.4 GHz where the onset of larger IL occurs. Three out of band resonances are present at 3.7 GHz, 3.9 GHz, and 4.3 GHz, as predicted in Fig. 3. An A0 passband at 0.8 GHz and an SH0 passband at 1.6 GHz are also measured. Different group delays are observed in the A1 and SH0 passbands as A1 is slower than SH0 in this frequency range. This validates that A1 features low v_g and high v_p simultaneously, thus promising compact device sizes with large feature sizes at 5 GHz.

IV. Conclusion

In this work, we have demonstrated A1 ADLs at 5 GHz in $LiNbO_3$ thin films for the first time. Thanks to the fast v_p, high k^2, and low loss of A1, the operating frequency significantly surpasses the state-of-the-art in ADLs with similar feature sizes. The key design parameters are identified, and their effects

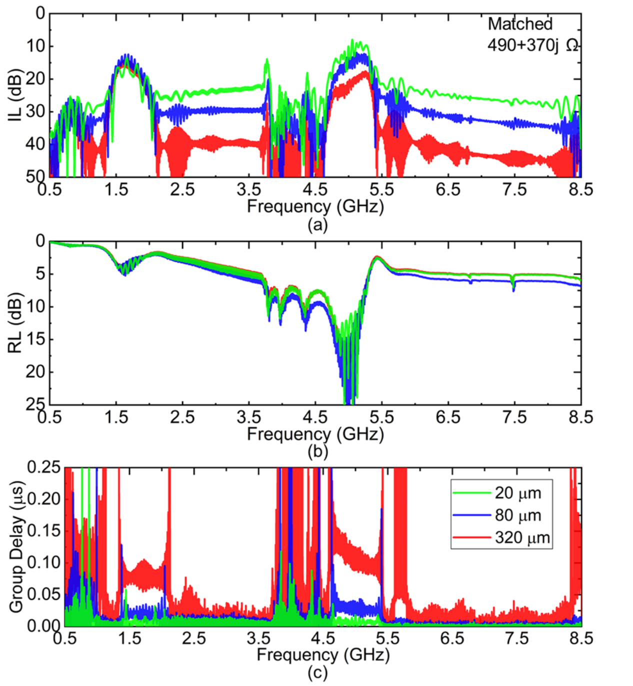

Fig. 6. Measured wideband performance of the devices in Group A: (a) IL, (b) RL, and (c) group delay.

on the performance are discussed. The implemented ADLs at 5 GHz show a minimum insertion loss of 7.9 dB, and a fractional bandwidth around 4%, with delays ranging between 15 ns and 109 ns. Upon further optimization, the A1 ADLs can lead to wide-band and high-frequency signal processing functions for 5G applications.

Acknowledgment

The authors would like to thank the DARPA MTO NZERO and SPAR programs for funding support and Dr. Troy Olsson for helpful discussions.

References

[1] S. Parkvall, E. Dahlman, A. Furuskar, and M. Frenne, "NR: The new 5G radio access technology," *IEEE Commun. Stand. Mag.*, vol. 1, no. 4, pp. 24–30, 2017.

[2] P. Popovski, K. F. Trillingsgaard, O. Simeone, and G. Durisi, "5G Wireless Network Slicing for eMBB, URLLC, and mMTC: A Communication-Theoretic View," *IEEE Access*, vol. 6, pp. 55765–55779, 2018.

[3] R. Ruby, "A snapshot in time: The future in filters for cell phones," *IEEE Microw. Mag.*, vol. 16, no. 7, pp. 46–59, 2015.

[4] M. Kadota, Y. Ishii, and S. Tanaka, "Ultra-wideband T-and π-type ladder filters using a fundamental shear horizontal mode plate wave in a LiNbO3 plate," *Jpn. J. Appl. Phys.*, vol. 58, no. SG, p. SGGC10, 2019.

[5] A. Kochhar *et al.*, "Resonant Microelectromechanical Receiver," *J. Microelectromechanical Syst.*, vol. 28, no. 3, pp. 327–343, 2019.

[6] R. Lu, T. Manzaneque, Y. Yang, and S. Gong, "Lithium Niobate Phononic Crystals for Tailoring Performance of RF Laterally Vibrating Devices," *IEEE Trans. Ultrason. Ferroelectr. Freq. Control*, vol. 65, no. 6, pp. 934–944.

[7] R. Lu, T. Manzaneque, Y. Yang, J. Zhou, H. Hassanieh, and S. Gong, "RF Filters with Periodic Passbands for Sparse Fourier Transform-based Spectrum Sensing," *J. Microelectromechanical Syst.*, vol. 27, no. 5, pp. 931–944, 2018.

[8] M. M. Torunbalci, S. Sridaran, R. C. Ruby, and S. A. Bhave, "Mechanically Modulated Microwave Circulator," in *Transducers*, 2019, pp. 713–716.

[9] T. Kimura, M. Omura, Y. Kishimoto, and K. Hashimoto, "Comparative Study of Acoustic Wave Devices Using Thin Piezoelectric Plates in the 3-5-GHz Range," *IEEE Trans. Microw. Theory Techn.*, vol. 67, no. 3, pp. 915–921, 2019.

[10] C. Cassella, Y. Hui, Z. Qian, G. Hummel, and M. Rinaldi, "Aluminum nitride cross-sectional Lamé mode resonators," *J. Microelectromechanical Syst.*, vol. 25, no. 2, pp. 275–285, 2016.

[11] L. Colombo, A. Kochhar, G. Vidal-Álvarez, and G. Piazza, "X-Cut Lithium Niobate Laterally Vibrating MEMS Resonator With Figure of Merit of 1560," *J. Microelectromechanical Syst.*, vol. 27, no. 4, pp. 602–604, 2018.

[12] T. Takai *et al.*, "High-performance SAW resonator on new multilayered substrate using LiTaO 3 crystal," *IEEE Trans. Ultrason. Ferroelectr. Freq. Control*, vol. 64, no. 9, pp. 1382–1389, 2017.

[13] M. Park, Z. Hao, D. G. Kim, A. Clark, R. Dargis, and A. Ansari, "A 10 GHz Single-Crystalline Scandium-Doped Aluminum Nitride Lamb-Wave Resonator," in *Transducers*, 2019, pp. 450–453.

[14] C. S. Hartmann and B. P. Abbott, "Overview of design challenges for single phase unidirectional SAW filters," in *IEEE Int. Ultrason. Symp*, 1989, pp. 79–89.

[15] S. Lehtonen, V. P. Plessky, C. S. Hartmann, and M. M. Salomaa, "SPUDT filters for the 2.45 GHz ISM band," *IEEE Trans. Ultrason. Ferroelectr. Freq. Control*, vol. 51, no. 12, pp. 1697–1703, 2004.

[16] T. Manzaneque, R. Lu, Y. Yang, and S. Gong, "Lithium Niobate MEMS Chirp Compressors for Near Zero Power Wake-Up Radios," *Journal of Microelectromechanical Systems*, pp. 1204–1215, 2017.

[17] S. Ghosh, M. A. Hollis, and R. J. Molnar, "Acoustoelectric amplification of Rayleigh waves in low sheet density AlGaN/GaN heterostructures on sapphire," *Appl. Phys. Lett.*, vol. 114, no. 6, p. 63502, 2019.

[18] L. Hackett *et al.*, "High-gain leaky surface acoustic wave amplifier in epitaxial InGaAs on lithium niobate heterostructure," *Appl. Phys. Lett.*, vol. 114, no. 25, p. 253503, Jun. 2019.

[19] R. Lu, T. Manzaneque, Y. Yang, L. Gao, A. Gao, and S. Gong, "A Radio Frequency Nonreciprocal Network Based on Switched Acoustic Delay Lines," *IEEE Trans. Microw. Theory Techn.*, vol. 67, no. 4, pp. 1516–1530, 2019.

[20] M. Kadota, Y. I. Yunoki, T. Shimatsu, M. Uomoto, and S. Tanaka, "Suprious-Free, Near-Zero-TCF Hetero Acoustic Layer (HAL) SAW Resonators Using LiTaO 3 Thin Plate on Quartz," in *IEEE Int. Ultrason. Symp.*, 2018, pp. 1–9.

[21] T. Manzaneque, R. Lu, Y. Yang, and S. Gong, "Low-Loss and Wideband Acoustic Delay Lines," *IEEE Trans. Microw. Theory Techn.*, vol. 67, no. 4, pp. 1379–1391, 2019.

[22] R. Lu, T. Manzaneque, Y. Yang, M.-H. Li, and S. Gong, "Gigahertz Low-Loss and Wide-Band S0 Mode Lithium Niobate Acoustic Delay Lines," *IEEE Trans. Ultrason. Ferroelectr. Freq. Control*, vol. 66, no. 8, pp. 1373–1386, 2019.

[23] R. H. Olsson *et al.*, "A high electromechanical coupling coefficient SH0 Lamb wave lithium niobate micromechanical resonator and a method for fabrication," *Sensors Actuators A Phys.*, vol. 209, pp. 183–190, 2014.

[24] R. Wang, S. A. Bhave, and K. Bhattacharjee, "Design and fabrication of S0 Lamb-wave thin-film lithium niobate micromechanical resonators," *J. Microelectromechanical Syst.*, vol. 24, no. 2, pp. 300–308, 2015.

[25] Y. Yang, A. Gao, R. Lu, and S. Gong, "5 GHz lithium niobate MEMS resonators with high FoM of 153," in *IEEE Int. Conf. Micro Electro Mech. Syst*, 2017, pp. 942–945.

[26] V. Plessky, S. Yandrapalli, P. J. Turner, L. G. Villanueva, J. Koskela, and R. B. Hammond, "5 GHz laterally-excited bulk-wave resonators (XBARs) based on thin platelets of lithium niobate," *Electron. Lett.*, vol. 55, no. 2, pp. 98–100, 2018.

[27] Y. Yang, R. Lu, L. Gao, and S. Gong, "4.5 GHz Lithium Niobate MEMS Filters with 10% Fractional Bandwidth for 5G Front-ends," *J. Microelectromechanical Syst.*, vol. 28, no. 4, pp. 575–577, 2019.

[28] Y. Yang, R. Lu, and S. Gong, "Scaling Acoustic Filters Towards 5G," in *IEEE International Electron Devices Meeting (IEDM)*, 2018, pp. 36–39.

[29] M. Faizan *et al.*, "Fabrication Of Lithium Niobate Bulk Acoustic Resonator For 5G Filters," in *Transducers*, 2019, pp. 1752–1755.

[30] R. Lu, M.-H. Li, Y. Yang, T. Manzaneque, and S. Gong, "Accurate Extraction of Large Electromechanical Coupling in Piezoelectric MEMS Resonators," *J. Microelectromechanical Syst.*, vol. 28, no. 2, pp. 209–218, 2019.